Experimental Investigation of Variations in Polycrystalline $Hf_{0.5}Zr_{0.5}O_2$ (HZO)-Based MFIM

Tae Ryong Kim, Revanth Koduru, Zehao Lin, *Member, IEEE*, Peide D. Ye, *Fellow, IEEE*, and Sumeet Kumar Gupta, *Senior Member, IEEE*

***Abstract*— Device-to-device variations in ferroelectric (FE) hafnium oxide (HfO_2)-based devices pose a crucial challenge that limits the otherwise promising capabilities of this technology. Previous simulation-based studies have identified polarization (P) domain nucleation and polycrystallinity as key contributors to variations in HfO_2; however, experimental validation remains limited. Here, we experimentally investigate variations in remanent charge (Q_R) of $Hf_{0.5}Zr_{0.5}O_2$ (HZO)-based metal–FE–insulator–metal (MFIM) capacitors across different set voltages (V_{SET}) and FE layer thicknesses (T_{FE}). Our measurements reveal a nonmonotonic behavior of the standard deviation of Q_R ($\sigma(Q_R)$) with V_{SET} peaking near coercive voltage (V_C), which is consistent with previous simulation-based predictions. In the low- and high-V_{SET} regions, Q_R variations are primarily dictated by saturation charge (Q_S) variations, which in turn, mainly originate from charge trap effects at the FE–dielectric (DE) interface and the polycrystallinity of FE. On the other hand, at the mid-V_{SET} region peak, the Q_R variations are attributed to the V_C variations, which arise from an additional (and dominant) effect of multidomain (MD) P switching. Notably, sharp P switching associated with domain nucleation amplifies the variations, resulting in a peak of Q_R variations in this V_{SET} range. Furthermore, we observe that as HZO thickness (T_{FE}) is scaled down, the nonmonotonicity in variations with V_{SET} is reduced, primarily due to reduced domain nucleation and smaller grain sizes. We experimentally establish a strong correlation of Q_R with Q_S in the low- and high-V_{SET} regions and with V_C in the mid-V_{SET} region across various T_{FE}. Finally, our experimental findings are corroborated by simulations using a 3-D phase-field model.**

***Index Terms*— Charge trapping, device-to-device variations, domain nucleation, ferroelectric (FE) layer thickness, $Hf_{0.5}Zr_{0.5}O_2$ (HZO), polycrystallinity, set voltage.**

I. Introduction

FERROELECTRIC (FE) materials are considered promising candidates for nonvolatile memory applications due to their electric-field driven low power write and other unique characteristics [1], [2], [3], [4]. The discovery of ferroelectricity in doped hafnium oxide (HfO_2) has triggered immense attraction by virtue of its CMOS compatibility [5], [6]. This has led to the integration of HfO_2 in various devices, such as ferroelectric RAM (FERAM) [7], [8], FE field effect transistors (FEFETs) [6], [9], and ferroelectric tunnel junctions (FTJs) [10], [11] and their use in a range of applications [1], [2], [3], [4]. Among various dopants for HfO_2 (Si [12], Al [13], Y [14], and La [15]) [16], Zirconium (Zr) stands out for its lower annealing temperature (400 °C) required for FE properties [17], [18]. A low thermal budget facilitates the integration of Zr-doped HfO_2 (HZO) with front-end-of-line (FEOL) conventional CMOS devices without introducing additional stress [18].

Despite their potential, several challenges hinder the commercialization of FE HZO devices [19], [20], [21], [22], [23], [24], [25]. Among these, device-to-device variations significantly impact the performance of HZO-based systems [21], [22], [23], [24], [25], [26]. In particular, in the context of multistate storage [multiple intermediate polariaztion (P)] [27], [28], [29], where the state of FE-based devices is determined by applied set voltage (V_{SET}) (or reset voltage (V_{RESET})), device-to-device variations are shown to be significantly dependent on V_{SET} (or V_{RESET}) [24], [25]. For example, the read current [24] and threshold voltage [25] of FEFET, determined by the remanent charge (Q_R) of the FE layer in the gate-stack, have been experimentally shown to display nonmonotonic dependence on V_{SET} (or V_{RESET}).

Several factors have been suggested as causes of these variations in HZO-based metal–FE–insulator–metal (MFIM), including polycrystallinity [30], [31], [32], multidomain (MD) P switching [33], [34], [35], and the charge trap effects at the FE–insulator or dielectric (DE) interface [36], [37], [38]. Multiple simulation-based studies have highlighted the role of polycrystallinity and MD P switching in governing the trends in the variations of coercive voltage (V_C) and Q_R from the standpoint of HZO-based MFIM capacitors [34], [35]. The variations in P switching in polycrystalline HZO devices are attributed to the dependence of Q_R and V_C on the crystal orientation angle of the grains [34] as well as the phase stabilization between orthorhombic (o-) and tetragonal (t-) phases [32], [39], [40]. MD P switching, prevalent in HZO due to its low gradient energy [33], is another crucial factor dictating variations due to its random nature (especially domain nucleation) [35]. Based on the phase-field simulations, the works in [34], [35], and [41] have shown that P switching

Received 14 January 2026; accepted 30 January 2026. Date of publication 10 March 2026; date of current version 26 March 2026. This work was supported in part by the National Science Foundation (NSF); and in part by the Center for the Co-Design of Cognitive Systems (COCOSYS), one of the seven centers in Joint University Microelectronics Program (JUMP) 2.0, funded by the Semiconductor Research Corporation (SRC) and Defense Advanced Research Projects Agency (DARPA). The review of this article was arranged by Editor C. Wu. *(Corresponding author: Tae Ryong Kim.)*

The authors are with the Elmore Family School of Electrical and Computer Engineering, Purdue University, West Lafayette, IN 47907 USA (e-mail: kim3804@purdue.edu; kodurur@purdue.edu; lin1174@purdue.edu; yep@purdue.edu; guptask@purdue.edu).

Digital Object Identifier 10.1109/TED.2026.3661370

1557-9646 © 2026 IEEE. All rights reserved, including rights for text and data mining, and training of artificial intelligence and similar technologies. Personal use is permitted, but republication/redistribution requires IEEE permission.
See https://www.ieee.org/publications/rights/index.html for more information.
Authorized licensed use limited to: Purdue University. Downloaded on April 06,2026 at 18:00:14 UTC from IEEE Xplore. Restrictions apply.

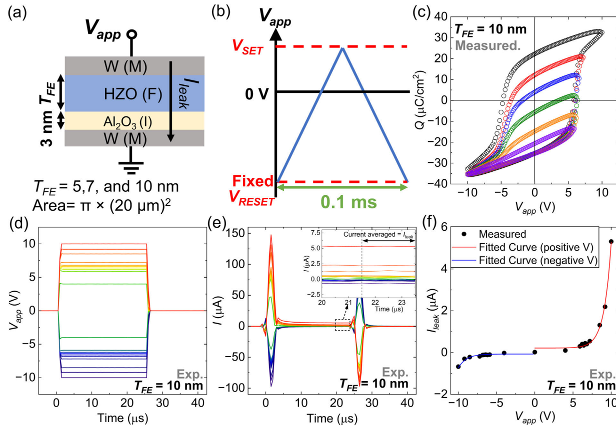

Fig. 1. (a) Schematic of the fabricated HZO-based MFIM capacitor. (b) Waveform of 10-kHz applied voltage (V_{app}). (c) Measured Q–V curves averaged over 50 MFIM capacitors with 10 nm of FE layer thickness (T_{FE}) for different set voltage (V_{SET}). (d) Waveform of pulses with various amplitudes for leakage current measurement and (e) their corresponding current response and the definition of leakage current (I_{leak}) in steady state (inset: zoomed-in view of I around 20–23.5 μs). (f) Measured I_{leak} for different voltages and its fit curves.

mechanisms (domain nucleation and domain growth) and domain characteristics are V_{SET} and T_{FE}-dependent, which causes Q_R variations to depend on V_{SET} and T_{FE} strongly. Despite these insights from simulations, experimental validation of these trends, especially with regard to T_{FE}, is limited. Moreover, exploring the correlation of variations with factors (like domain nucleation, polycrystallinity, and traps) is crucial for advancing the understanding of device-to-device variations in HZO devices.

This work experimentally characterizes the variations in Q_R as a function of V_{SET} and T_{FE} and provides evidence that aligns with previous simulation-based analyses and insights. By measuring Q_R from charge–voltage (Q–V) characteristics across 50 MFIM capacitors, each for three different T_{FE}, we capture the relation between Q_R, V_{SET}, and T_{FE}. The key contributions of this work are summarized below.

1) We experimentally establish that the standard deviation of Q_R ($\sigma(Q_R)$) exhibits a nonmonotonic trend with respect to V_{SET}, peaking at V_{SET} near V_C.
2) Our measurement results reveal that the $\sigma(Q_R)$ depends on T_{FE}, exhibiting distinct trends across low-, mid-, and high-V_{SET} ranges.
3) By analyzing the correlation between Q_R, V_C, and saturation charge (Q_S) measured across different V_{SET} and T_{FE}, we discuss the role of polycrystallinity, charge trapping effect, and domain nucleation in dictating the Q_R variations.
4) We support our experimental findings with the interpretations from our in-house 3-D phase-field model.

II. MFIM Capacitor Fabrication and Measurements

We fabricate HZO-based MFIM capacitors comprising 70-nm tungsten (W) for the top and bottom metal electrodes, an FE HZO layer with various thicknesses (T_{FE} = 5, 7, 10 nm), and a 3-nm Al_2O_3 DE layer, as shown in Fig. 1(a). The DE layer in the MFIM stack passivates the HZO/electrode interface [42] and suppresses trap-assisted leakage [43], improving reliability. In addition, the DE layer provides a depolarization field across the FE layer, which is exploited in multiple applications such as FTJ [44]. A thickness of 3-nm balances interface passivation/leakage blocking with strong capacitive coupling to HZO, providing an effective barrier without weakening FE switching [36], [45].

The MFIM fabrication process is as follows. First, the W bottom electrode is deposited on a bare Si wafer using sputtering. Atomic layer deposition (ALD) is then utilized to deposit HZO and Al_2O_3 layers at 200 °C. Following this, W is sputtered to form the top electrode. This is followed by 30 s of rapid thermal annealing (RTA) at 300 °C in the nitrogen (N_2) atmosphere. The capacitor area is defined by the top electrode, patterned as a circle with a 20-μm radius via photolithography and lift-off. Because of this relatively large device area, any marginal dimensional variation introduced during the lithography or lift-off process is negligible compared to the total capacitor area and does not meaningfully influence the extracted P values or their variation characteristics. Moreover, any area variation would result in only V_{SET}-independent scaling of the extracted measured Q_{R+}, thus having no impact on the nonmonotonic V_{SET}-dependent variation trends, discussed in this work.

The Q–V measurements of 50 fabricated MFIM capacitors for each T_{FE} are performed using a Radiant Premier II FE Tester through a probe station. The applied voltage (V_{app}) is swept at 10-kHz frequency from a fixed V_{RESET} to different V_{SET} values [see Fig. 1(b)]. Note that this biasing scheme is consistent with the programming methodology used in previous experimental works such as [27]. Moreover, it is notable that the voltage ramp rate change due to different V_{SET} has a negligible impact on Q–V hysteresis and V_C, as shown in Fig. 2(a). For consistency, V_{RESET} for each T_{FE} is selected to obtain a similar magnitude of average electric field (E-field) across the FE layer at V_{RESET} (= −10.0, −8.3, and −7.1 V for T_{FE} = 10, 7, and 5 nm). (Note: the E-field is estimated by using phase-field simulations.) To reduce the effect of cycle-to-cycle variations [34], the Q–V curves used in the analysis are averaged over five measurement cycles. The Q–V loops (including major and minor loops) reach different Q_R values depending on V_{SET} [see Fig. 1(c)].

To mitigate the influence of static leakage current (I_{leak}) through the MFIM stack [see Fig. 1(a)], we perform a separate leakage measurement and subtract leakage charge (Q_{leak}) from the measured Q–V for each individual MFIM sample. (Note, we do not use the PUND technique to eliminate leakage since it also eliminates other components of charge, such as the nonswitching DE component, which we want to keep in our study). For the leakage measurement, we first apply voltage pulses (25 μs) of varying amplitudes to each MFIM capacitor [see Fig. 1(d)]. I_{leak} is measured during a stable time frame where the transient current has decayed [see Fig. 1(e)]. To obtain the Q_{leak} over the V_{app} sweep duration that needs to be deducted from the measured Q–V, we need to integrate I_{leak} for the time window during which V_{app} is applied for the Q–V measurements. We calculate Q_{leak} using in the following

Authorized licensed use limited to: Purdue University. Downloaded on April 06,2026 at 18:00:14 UTC from IEEE Xplore. Restrictions apply.

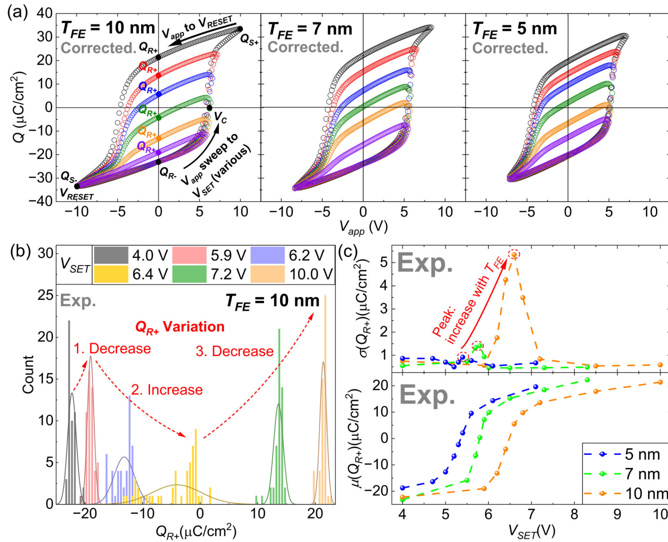

Fig. 2. (a) Corrected Q–V curves averaged over 50 MFIM capacitors with T_{FE} = 10, 7, and 5 nm for different V_{SET}, (b) Q_{R+} distribution for 50 MFIM capacitors with T_{FE} = 10 nm at different V_{SET}, and (c) standard deviation (σ) and mean (μ) of Q_{R+} ($\sigma(Q_{R+})$ and $\mu(Q_{R+})$, respectively) versus V_{SET} for T_{FE} = 5, 7, and 10 nm.

equation:

$$Q_{leak}(V(t)) = \int_0^t I_{leak}(V(\tau))\, d\tau \tag{1}$$

where I_{leak} is fit to the measured data [see Fig. 1(f)] based on an exponential equation given below

$$I_{leak}(V) = I_0 + Ae^{\mathrm{BV}}. \tag{2}$$

This is a phenomenological model consistent with established leakage physics, such as WKB tunneling through thin oxides [46] and field-enhanced trap-assisted tunneling [47].

Fig. 2(a) illustrates the Q–V plots (with leakage component removed) averaged for the 50 MFIM capacitors for T_{FE} = 10, 7, and 5 nm for various V_{SET}. All these curves start from negative Q_S (Q_{S-}) at the fixed V_{RESET}, pass negative Q_R (Q_{R+}) at V_{app} = 0 V, and reach varying Q values depending on V_{SET}. After that, Q returns to Q_{S-} as V_{app} is swept backward from V_{SET} to V_{RESET}. Note, the Q–V curves reach positive Q_S (Q_{S+}) only for the major loop, where $|V_{SET}| = |V_{RESET}|$.

The positive Q_R (Q_{R+}) is measured at V_{app} = 0 V on the return path from V_{SET} to V_{RESET} for each cycle. V_C is extracted as the voltage where Q = 0 μC/cm^2 on the path from V_{RESET} to V_{SET} in the major loop. Note that we consider the scenario where different V_{SET} values are applied to achieve multiple states of the MFIM from an initial fixed reset state (spontaneous state after the application of fixed V_{RESET}). We characterize the standard deviation of Q_{R+} ($\sigma(Q_{R+})$) to analyze the device-to-device variations in Q_{R+}. Note, analyzing Q_{R-} for different V_{RESET} (after the application of fixed V_{SET} application) is equivalent to our analysis. Hence, here, we focus on the trends in Q_{R+} variations.

III. Experimental Results

A. Non-Monotonic Trend of Q_{R+} Variations With V_{SET}

Fig. 2(b) shows the measured Q_{R+} distributions for 50 MFIM capacitors with T_{FE} = 10 nm at various V_{SET} values, revealing a significant dependence of Q_{R+} variations on V_{SET}. $\sigma(Q_{R+})$ shows a nonmonotonic behavior with respect to V_{SET} (as also predicted via simulations in [35]). Initially, the distribution shows a mild reduction in $\sigma(Q_{R+})$ as V_{SET} increases from 4.0 to 5.9 V (region-1 or low-V_{SET} range). The distribution substantially increases its spread as V_{SET} increases from 5.9 to 6.4 V (region-2 or mid-V_{SET} range). As V_{SET} increases further, $\sigma(Q_{R+})$ reduces (region-3 or high-V_{SET} range), followed by a slight increase as V_{SET} is increased further. It can be observed in Fig. 2(c) that $\sigma(Q_{R+})$ exhibits a peak at a particular V_{SET}, which is annotated as V_{peak}. Given that the mean Q_{R+} ($\mu(Q_{R+})$) at V_{peak} is close to 0 μC/cm^2 [see Fig. 2(c)], it follows that $\sigma(Q_{R+})$ reaches a peak point around $V_{SET} \sim V_C$.

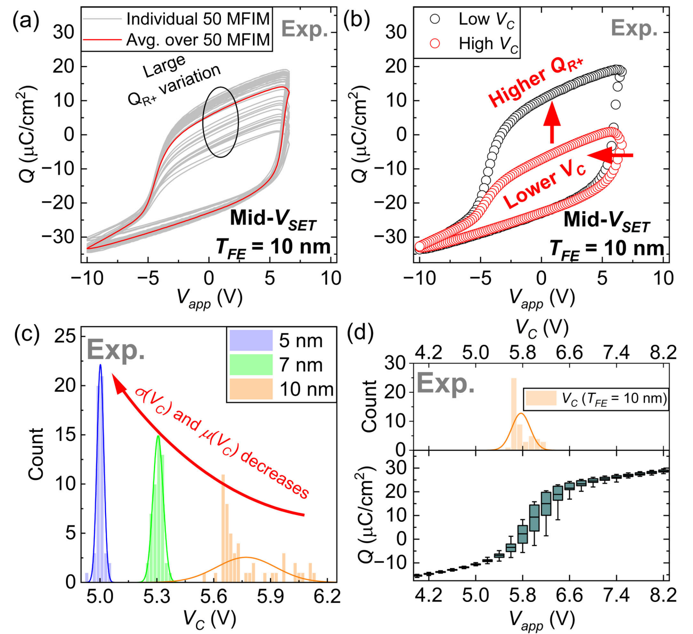

Fig. 3. (a) Q–V curves of individual and averaged 50 MFIM capacitors with T_{FE} = 10 nm at V_{SET} = 6.6 V. (b) Q–V minor loops (V_{SET} = 6.6 V) with different V_C. At V_{SET} range around V_C, Q_{R+} is largely dependent on V_C. (c) Measured V_C distribution from 50 MFIM capacitors of different T_{FE}. (d) Measured V_C distribution (top) and box plot depicting the Q variations around V_C (bottom) of 50 MFIM with T_{FE} = 10 nm.

With decreasing T_{FE}, the nonmonotonicity of $\sigma(Q_{R+})$ becomes less prominent, with the peak value of $\sigma(Q_{R+})$ decreasing as T_{FE} scales down. We report the peak value reducing from 5.34 μC/cm^2 at T_{FE} = 10 nm to 1.41 μC/cm^2 (0.26×) and 0.71 μC/cm^2 (0.17×) at T_{FE} = 7 and 5 nm. To understand this reduction, we plot the measured V_C distributions in Fig. 3(c). We observe a decrease in V_C variations as T_{FE} decreases. Since Q_{R+} variations are largely influenced by V_C in the mid-V_{SET} range [see Fig. 3(b)], Q_R variations also decrease with T_{FE} scaling. Compared to T_{FE} = 10 nm, $\sigma(V_C)$ reduces to 0.17× at T_{FE} = 7 nm and 0.12× at T_{FE} = 5 nm. Therefore, we can correlate a decrease in the peak $\sigma(Q_{R+})$ primarily with lower V_C variations at a scaled T_{FE}. Also, the V_C distributions explain the V_{peak} shift toward lower V_{SET}. The mean value of V_C ($\mu(V_C)$) shows a shift to a lower value as T_{FE} is scaled (5.8 → 5.3 → 5.0 V for T_{FE} = 10, 7, and 5 nm). This is primarily due to an increase in E-field for lower T_{FE} at a given V_{app}. This aligns with V_{peak} shifts shown in Fig. 2(b) (6.6 → 5.8 → 5.4 V for T_{FE} = 10, 7, and

Authorized licensed use limited to: Purdue University. Downloaded on April 06,2026 at 18:00:14 UTC from IEEE Xplore. Restrictions apply.

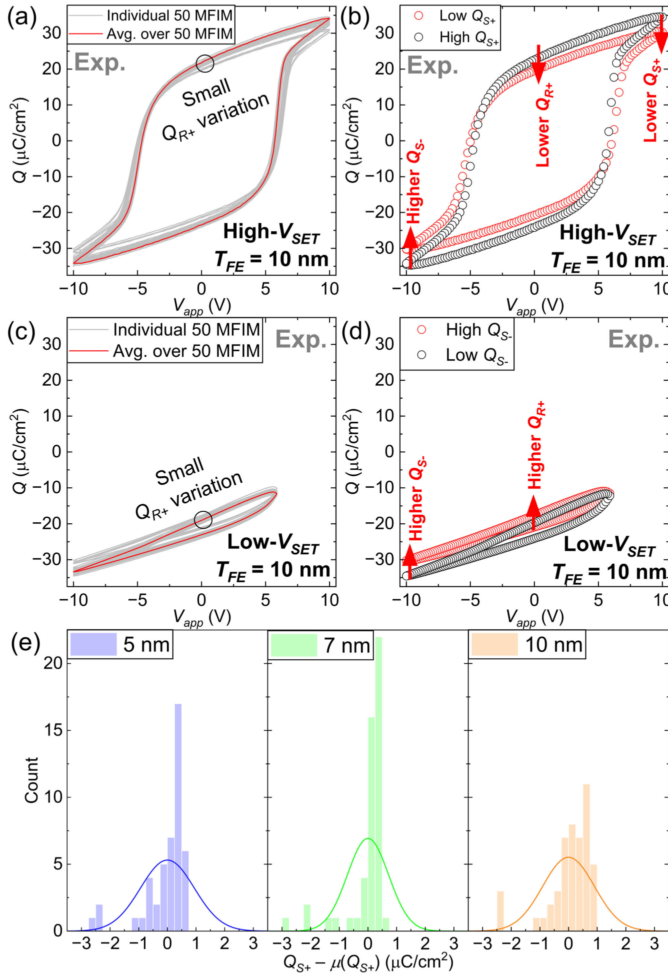

Fig. 4. Q–V curves of individual and averaged 50 MFIM capacitors at (a) V_{SET} = 10.0 V and (c) V_{SET} = 5.9 V. (b) Q–V major loops (V_{SET} = 10.0 V) with different Q_{S+}. (d) Q–V minor loops (V_{SET} = 5.9 V) with different Q_{S-}. In the high-V_{SET} range, Q_{R+} is largely dependent on Q_{S+}, and Q_{S-} is negatively correlated with Q_{S+}. (e) Distribution of Q_{S+}–$\mu(Q_{S+})$ from 50 MFIM capacitors of different T_{FE}. The $\sigma(Q_{R+})$ trends in Fig. 2(c) at the low and high-V_{SET} range follow that of the Q_{S+} distribution.

5 nm). These results illustrate that V_{peak} is linked to V_C and decreases as T_{FE} is scaled. Furthermore, as T_{FE} scales, a pronounced "W"-shaped nonmonotonicity with two local minima is observed in the $\sigma(Q_{R+})$-V_{SET} plot, which will be discussed in more detail later.

However, $\sigma(Q_{R+})$ in low- and high-V_{SET} regions does not display any trend depending on T_{FE} (unlike in mid-V_{SET}). In these regions, $\sigma(Q_{R+})$ is the highest for T_{FE} = 5 nm, followed by 10 and 7 nm for both low- and high-V_{SET} regions [see Fig. 2(c)].

To understand the trend in the high-V_{SET} regions, let us look at Fig. 4(b), which points to a relationship between Q_{S+} variations and Q_{R+} variations. In particular, MFIM samples with lower Q_{S+} are likely to exhibit lower Q_{R+}. Measured Q_{S+} distributions for each T_{FE} in Fig. 4(e) show that the variation is the largest for T_{FE} = 5 nm, followed by 10 and 7 nm, reflecting the trend observed in Q_{R+} variations in the high-V_{SET} region.

In the low-V_{SET} region, two key factors dictate Q_{R+} variations. First, lower (more negative) Q_{S-} results in a lower Q_{R+}, as shown in Fig. 4(c), indicating that the variations in Q_{S-} directly drive Q_{R+} variations. Second, because Q_{S-} (< 0) and Q_{S+} (> 0) are both governed by similar mechanisms associated with interface-traps and polycrystallinity, the two quantities are correlated across devices. In particular, a higher interface trap density increases the charge magnitude via two mechanisms: 1) direct charge addition, where a higher magnitude of trapped charge (Q_{it}) (positive for V_{app} > 0 and negative for V_{app} < 0) increases both $|Q_{S+}|$and $|Q_{S-}|$ due to charge balance ($Q_{FE} \simeq Q_{DE} + Q_{it}$ where $Q_{FE/DE}$ is the Q across FE/DE layer) [36]; and 2) E-field enhancement, where more trapped charges increase the effective E-field across the FE layer (due to lower Q_{DE} and depolarization field), leading to larger $|Q_S|$ (details in Section IV-A). In addition, polycrystalline factors, such as lower grain angle (θ) or higher o-phase fraction, yield larger Q magnitude. Accordingly, $|Q_{S+}|$ and $|Q_{S-}|$ exhibit a positive correlation, which means that a more positive Q_{S+} corresponds to a more negative Q_{S-} [see Fig. 4(b)]. In other words, a negative correlation is established between Q_{S+} and Q_{R+}, where a larger value of Q_{S+} is associated with a smaller (more negative) value of Q_{S-}, which, in turn, leads to a smaller value of Q_{R+} in the low-V_{SET} region. Furthermore, the consistency in the trend of $\sigma(Q_{R+})$ and $\sigma(Q_{S+})$ with respect to T_{FE} [see Fig. 4(d)] substantiates the correlation of Q_{S+} variations on Q_{R+} variations in the low-V_{SET} region.

B. Correlation Analysis for Q_{R+} With V_C and Q_{S+}

To further understand the relationships between Q_{R+}, V_C, and Q_{S+}, we present scatter plots in Fig. 5(a) showing the correlation of measured values of Q_{R+} with Q_{S+} and V_C across different V_{SET} values for 50 MFIM capacitors at T_{FE} = 10 nm. At low-V_{SET} (= 4.0 V), Q_{R+} shows a strong correlation with Q_{S+}, suggesting that Q_{R+} variations at the low-V_{SET} range are mainly driven by factors influencing Q_{S+}. As V_{SET} approaches the mid-V_{SET} range (close to V_C), the correlation between Q_{R+} and Q_{S+} becomes weaker [V_{SET} = 6.4 V in Fig. 5(a)]. With a further increase in V_{SET} (high-V_{SET} range), the correlation between Q_{R+} and Q_{S+} becomes strong again. Notably, Q_{R+} negatively correlates with Q_{S+} at the low-V_{SET} range (4.0 V), while it correlates positively at the high-V_{SET} range (10.0 V). At high-V_{SET}, MFIM with higher Q_{S+} yields higher Q_{R+}, as discussed in Section III-A, leading to a positive correlation. On the other hand, in the low-V_{SET} range, Q_{R+} is mainly determined by Q_{S-}, i.e., higher Q_{S-} (less negative Q_{S-}) yields higher Q_{R+}. Now, recalling the negative correlation between Q_{S-} and Q_{S+}, a higher (less negative) Q implies a lower Q_{S+}. As discussed before, by combining these two observations, we can deduce that lower Q_{S+} results in higher Q_{R+} in the low-V_{SET} range. This results in a negative correlation at V_{SET} = 4.0 V.

Now, let us discuss the correlation of Q_{R+} with V_C [see Fig. 5(b)]. In the low-V_{SET} range (V_{SET} = 4.0 V), Q_{R+} shows minimal correlation with V_C. As V_{SET} increases, approaching 6.4 V (mid-V_{SET}), a strong negative correlation emerges showing that capacitors with low V_C undergo higher P switching at a given V_{app}. In the high-V_{SET} range, the correlation becomes weak again, indicating a reduced influence of V_C on Q_{R+}.

Authorized licensed use limited to: Purdue University. Downloaded on April 06,2026 at 18:00:14 UTC from IEEE Xplore. Restrictions apply.

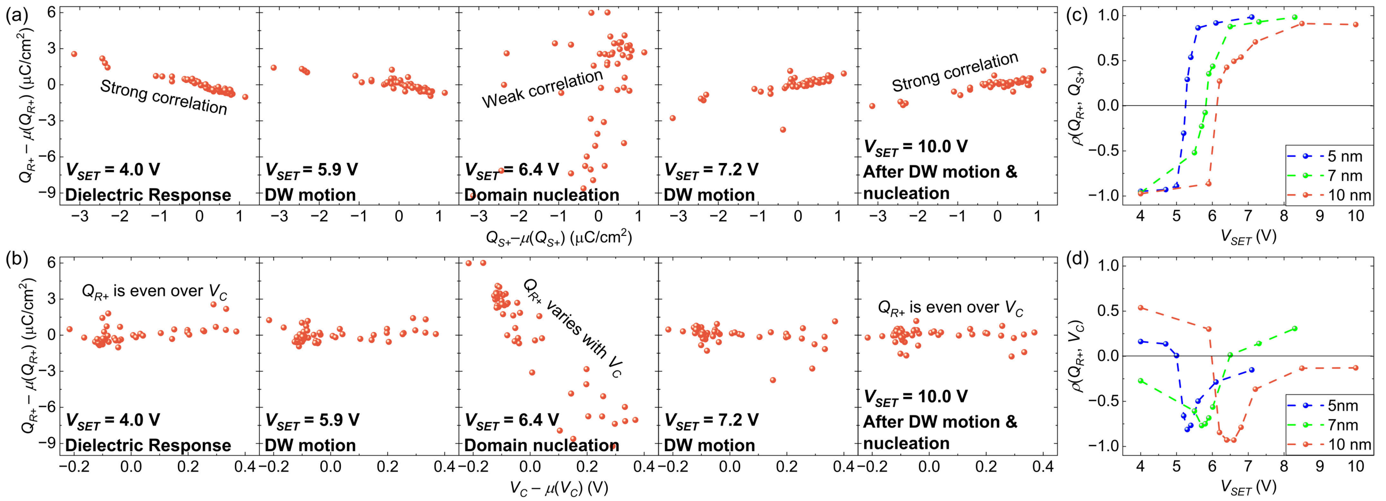

Fig. 5. Measured correlation plots of Q_{R+}–$\mu(Q_{R+})$ with (a) Q_{S+}–$\mu(Q_{S+})$ and (b) V_C–$\mu(V_C)$ of the 50 MFIM capacitors with T_{FE} = 10 nm and the correlation coefficient of Q_{R+} with (c) Q_{S+} ($\rho(Q_{R+}, Q_{S+})$) and (d) V_C ($\rho(Q_{R+}, V_C)$) as a function of V_{SET} for different T_{FE}.

The correlation coefficient (ρ) of Q_{R+} with Q_{S+} ($\rho(Q_{R+}, Q_{S+})$) [see Fig. 5(c)] and V_C ($\rho(Q_{R+}, V_C)$) [see Fig. 5(d)] across different V_{SET} values summarize the discussion above. Initially, $\rho(Q_{R+}, Q_{S+})$ is around −1, indicating a strong negative correlation. It approaches 0 at $V_{SET} \sim V_C$ and reaches +1 at the high-V_{SET} values. For $\rho(Q_{R+}, V_C)$, the coefficient dips to almost −1 around V_C, representing a substantial negative correlation, and remains closer to 0 at other V_{SET} values. We also observe that these trends hold for all T_{FE} (with some differences that will be discussed subsequently).

IV. Analysis of Q_{R+} Variation: Mechanisms for Different V_{SET} Ranges

A. Q_{R+} Variation Mechanism in the Low- and High-V_{SET} Regions

Here, we focus on three main mechanisms for Q_{R+} variations: MD P switching, polycrystallinity, and the charge trapping at the FE–DE interface. As we will discuss, MD P switching is not a major contributor to the variation in the low- and high-V_{SET} range due to small P switching in the former and nearly complete P switching in the latter region. Therefore, the primary influence on the variations comes from charge trapping [36], [37], [38], and polycrystallinity [34], [40]. The strong correlation between Q_{S+} and Q_{R+} observed experimentally confirms that the Q_{R+} variations are mainly driven by Q_{S+} variations [see Fig. 4(b) and (d)] originating from charge trap effects and polycrystallinity.

Charge trapping affects Q_{S+} variations through two mechanisms. First, trapped charges directly influence P within the FE layer [36], [37]. Second, trapped charges modify the depolarization field across the FE layer [48], resulting in a change in the domain wall (DW) density [41].

Apart from charge trapping, polycrystallinity is another key contributor to the Q_{S+} variations. In polycrystalline HZO, the grain orientation angle (θ)—the angle between the P direction (c-axis of the orthorhombic unit cell) and the physical out-of-plane axis—governs P switching. Since the component of the applied E-field along the c-axis contributes to switching [34], variations in θ among grains lead to a nonuniform P switching. In particular, grains with larger θ are stimulated with a weaker effective E-field, which leads to higher V_C. Due to the resultant suppressed P switching, a fraction of the original P domains remains even after the P switching in the major loop, leading to a reduction in Q_{S+} for higher θ [34]. In addition to the grain orientation angle effect, polycrystallinity also contributes to Q_{S+} variation through its impact on phase stabilization between o- and t-phases [40]. The t-phase lowers the overall Q_S and exhibits a higher DE constant [49] than the o-phase. This effect is particularly relevant as the t-phase is known to be stabilized by smaller grain sizes, which are more prevalent in thinner HZO films [40].

To investigate the impact of charge trapping, we analyze dQ/dV_{app} in voltage regions with minimal P switching and dominant DE response. Previous studies have shown that trapped charges at the FE–DE interface [36] result in different dQ/dV_{app} in the nonswitching region [37]. This effect is experimentally demonstrated in Fig. 6(a), which compares the Q–V characteristics of two MFIM capacitor samples in our study. One device shown with black symbols reaches a higher Q_{S+} for high-V_{SET}, indicating a higher trapped charge density compared to the other device (red symbols). Importantly, the device with a higher interface trap density (black symbols) exhibits a steeper slope of dQ/dV_{app} in the nonswitching region compared to the lower trap device (red symbols).

The plots in Fig. 6(b)–(d) confirm a positive correlation between Q_{S+} and dQ/dV_{app} across all T_{FE}. The most plausible origin of this positive correlation is interface charge trapping, while the contributions from MD P switching and polycrystallinity play a minor role in this specific trend. This can be understood as follows. First, switching in the low-V_{SET} region is minimal, and in the high-V_{SET} region where Q_{S+} is defined, most FE domains have already switched; therefore, the random component of MD switching is largely suppressed. Second, grain angle variations due to polycrystallinity do not affect dQ/dV_{app} to a significant extent since the background permittivity is independent of the c-axis orientation [34].

Authorized licensed use limited to: Purdue University. Downloaded on April 06,2026 at 18:00:14 UTC from IEEE Xplore. Restrictions apply.

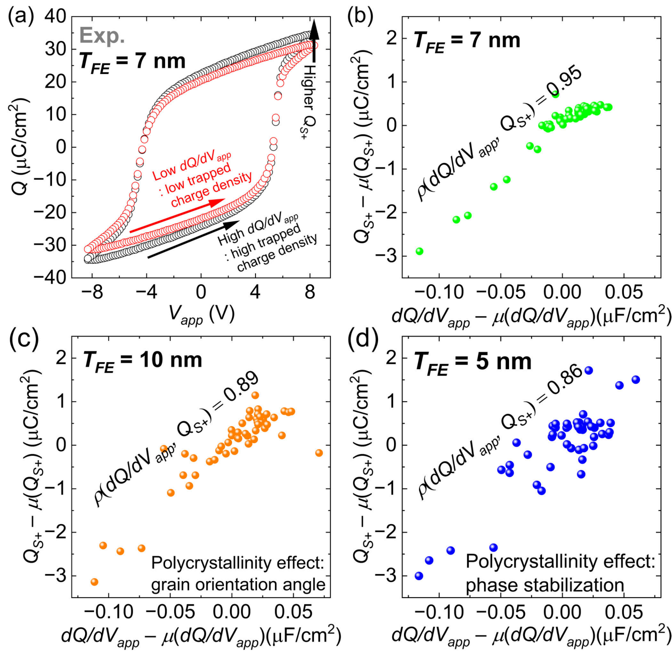

Fig. 6. (a) Q–V loops with different trapped charge densities. The black Q–V loop features higher dQ/dV_{app} and Q_{S+} than the red curve, representing a higher trapped charge density and the measured correlation plots of Q_{S+}–$\mu(Q_{S+})$ with dQ/dV_{app}–$\mu(dQ/dV_{app})$ for T_{FE} = (b) 7, (c) 10, and (d) 5 nm. For T_{FE} = 10 and 5 nm, polycrystallinity introduces additional variation to Q_{S+} and dQ/dV_{app}, reducing the correlation coefficient. At 10 nm, the effect of grain orientation angle is significant, whereas the phase distribution effect is large at 5 nm.

Third, variations in the t-phase fraction could affect both Q_{S+} and dQ/dV_{app}, but would tend to produce a negative correlation between Q_{S+} and dQ/dV_{app} since a higher t-phase fraction increases background permittivity while reducing the switchable P. This is inconsistent with the observed positive correlation between Q_{S+} and dQ/dV_{app}. In contrast, a higher trap density increases both Q_{S+} and dQ/dV_{app} because traps add charge and also modify the electrostatics of the FE–DE stack in a way that enhances the effective E-field across the FE layer. Therefore, the positive correlation in Fig. 6(b)–(d) highlights the significant role of charge trapping in governing Q_{S+} variations, which in turn contribute to Q_{R+} variations in the low- and high-V_{SET} ranges (as discussed in Fig. 5).

Although the interface charge trapping remains the dominant source of Q_{S+} variation, polycrystallinity does play some role, particularly at T_{FE} = 5 and 10 nm, leading to larger dispersion than T_{FE} = 7 nm. For T_{FE} = 10 nm (thickest HZO), the larger average grain size [30] results in the smaller number of grains (N_{grain}) within a fixed cross-sectional area; hence, the statistical averaging effect becomes less effective and the grain angle effect is more pronounced [26]. Grains with a large θ contribute to smaller out-of-plane P, reducing $|Q_S|$. Thus, the variations in the grain orientation angle increase the spread in the Q_{S+} [see Fig. 6(c)].

This dependence is further corroborated by the unique correlation observed for T_{FE} = 10 nm between Q_{R+} and V_C [see Fig. 5(d)]. Since increased θ leads to lower Q_{S+} and higher V_C, these two parameters exhibit a nonzero correlation when the grain angle effect becomes prominent. In the low-V_{SET} region, where Q_{R+} shows a significant negative correlation with Q_{S+}, this θ-driven correlation yields a positive $\rho(Q_{R+}, V_C)$. Experimentally, at the low-V_{SET}, devices with T_{FE} = 10 nm display $\rho(Q_{R+}, V_C)$ = 0.538, higher than that of T_{FE} = 7 nm (−0.272) and 5 nm (0.163) [see Fig. 5(d)].

Conversely, for T_{FE} = 5 nm, the polycrystallinity effect is dominated by phase stabilization rather than grain orientation. The reduced T_{FE} restricts grain growth, increasing the probability of stabilizing t-phase over the o-phase [40]. Because the t-phase exhibits a higher dQ/dV_{app} and lower Q_{S+}, device-to-device differences in the local o-/t-phase fraction introduce variations that oppose the trap-induced positive correlation. Therefore, the phase distribution is responsible for the larger dispersion observed in Fig. 6(d) for T_{FE} = 5 nm (compared to the other T_{FE} values).

It is notable that the charge trapping is a dominant source of Q_{S+} variation in this work. This can be attributed to the large cross-sectional area of our experimental MFIM samples (= $\pi\times$ (20 μm)^2), which makes the impact of N_{grain} on variations relatively less significant. However, for scaled devices, polycrystallinity can be a significant contributor, as has been shown in previous simulation studies [34].

B. Q_{R+} Variation Mechanisms in the Mid-V_{SET} Region

In the mid-V_{SET} range, Q_{R+} variations are mainly dictated by V_C variations as shown in the correlation plots [see Fig. 5(a)]. The sharp Q increase with increasing V_{app} in the mid-V_{SET} region amplifies V_C-induced Q_{R+} variations [see Fig. 3(a) and (d)], which leads to the $\sigma(Q_{R+})$ peaks as shown in Fig. 2(c). According to the previous simulation-based studies [34], [35], the strong influence of domain nucleation around the mid-V_{SET} range leads to large variations in Q_{R+}. Domain nucleation features inherent randomness and sharp P switching (a large amount of P switched in a small voltage range). The randomness of domain nucleation arises from the polycrystallinity of HZO and random MD P configurations [34], [35]. This leads to different samples nucleating at different V_{app}, represented by the V_C variations [see Fig. 3(c)]. Due to the sharp P switching associated with domain nucleation, a subset of samples with lower V_C (early nucleating samples) reaches a higher P at a given V_{app} [35]. As shown in Fig. 3(d), this effect broadens the P distribution around V_C due to the sharp P switching, and leads to large Q_{R+} variations [see Fig. 3(a)] as V_{app} returns from $V_{SET} \sim V_C$ to 0 V.

The impact of T_{FE} on $\sigma(Q_{R+})$ peaks is consistent with the attribution of polycrystallinity and MD effect on Q_{R+} variations. In a thinner FE layer, the $-P$ domain patterns become denser to compensate for increased depolarization energy [41]. This increased domain density limits the room for domain nucleation and thus suppresses it. Therefore, DW motion becomes a prevalent P switching mechanism in a thinner FE layer, leading to reduced randomness and, consequently, lower V_C [see Fig. 3(c)] and Q_{R+} variations [see Fig. 2(c)].

C. Origin of the "W"-Shaped $\sigma(Q_{R+})$ Dependence on V_{SET}

The observed nonmonotonic "W"-shaped dependence of $\sigma(Q_{R+})$ on V_{SET}, particularly evident in thinner HZO films (specifically, T_{FE} = 5 nm), arises from the interplay between

Authorized licensed use limited to: Purdue University. Downloaded on April 06,2026 at 18:00:14 UTC from IEEE Xplore. Restrictions apply.

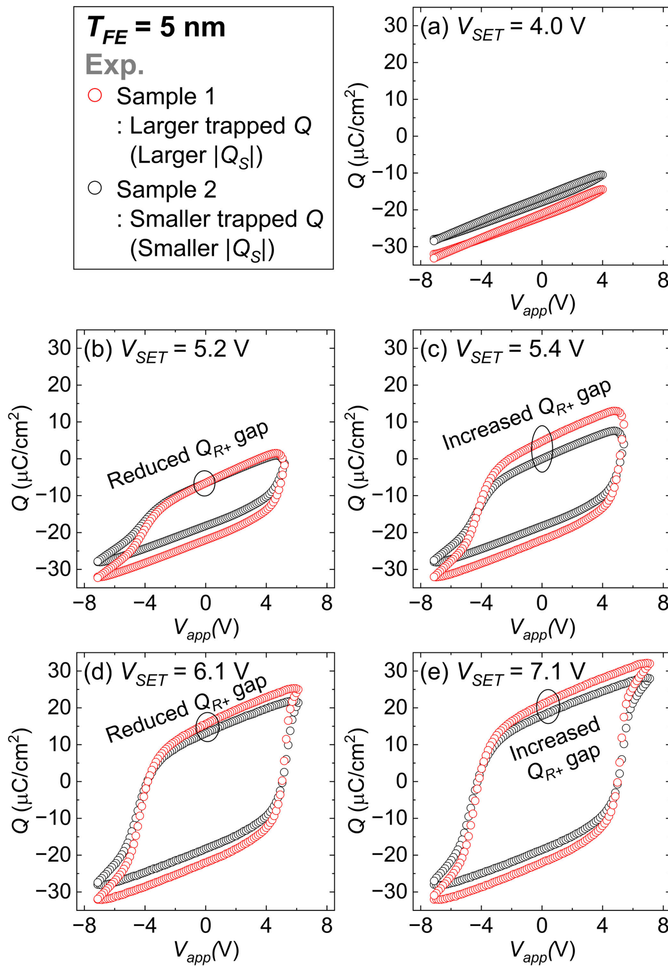

Fig. 7. Q–V hysteresis loops of two MFIM devices with T_{FE} = 5 nm exhibiting different charge trapping density (red: high/black: low) at V_{SET} = (a) 4.0, (b) 5.2, (c) 5.4, (d) 6.1, and (e) 7.1 V, illustrating the origin of the "W"-shaped $\sigma(Q_{R+})$ trend versus V_{SET}.

P switching dynamics (specifically, MD switching) and the electrostatic contributions of interface trapped charge. We can explain the four distinct regions of this "W"-shape: 1) initial decrease in variations at the low-V_{SET}, 2) subsequent increase at the mid-V_{SET} followed by a 3) decrease, and 4) final increase at high-V_{SET}—by considering two representative MFIM samples with different charge trapping density as shown in Fig. 7. In this comparison, Sample 1 (red) exhibits a larger $|Q_S|$ than Sample 2 (black), which indicates a higher interface trapped charge density for Sample 1.

First, in the low-V_{SET} region, P switching is minimal and primarily governed by DW motion. At V_{SET} = 4.0 V [see Fig. 7(a)], Sample 1 exhibits a larger $|Q_{S-}|$ due to higher trap density at the interface. This leads to larger $|Q_{R+}|$ due to the dominance of the nonswitching characteristics, with P switching being minimal at this voltage. The differences in the trap charges between Sample 1 and Sample 2 (and in general, all the samples) lead to some variations in Q_{R+}. At the same time, higher trapped charge density reduces the potential drop across the DE layer, resulting in a stronger E-field across the FE layer for Sample 1. Thus, when V_{SET} is increased to 5.2 V, the enhanced field in Sample 1 acts as a stronger driving field for DW motion, yielding larger P-switching at V_{SET} = 5.2 V than Sample 2 [see Fig. 7(b)]. This effect reduces the gap in Q_{R+} between the two samples (and in general, across the device population), resulting in the initial decrease in $\sigma(Q_{R+})$.

Second, as V_{SET} approaches the mid-V_{SET} region around V_C, (here, V_{SET} = 5.4 V), the dominant switching mechanism transitions to domain nucleation. Nucleation is an inherently random process, which significantly increases the variation in P switching and leads to the broadening of the Q_{R+} distribution as shown in Fig. 7(c).

Third, with a further increase in V_{SET} (V_{SET} = 6.1 V), the majority of P domains have switched as V_{app} surpasses the V_C range. This restricts random nucleation to a small number of remaining unswitched regions. As a result, the contribution of random nucleation diminishes, and the Q_{R+} values converge [see Fig. 7(d)], causing $\sigma(Q_{R+})$ to correspondingly decrease.

Finally, in the high-V_{SET} region (V_{SET} = 7.1 V), the variation increases once more. Because random P switching effects are greatly reduced in this region, the variation is driven again by the charge trapping effect. In particular, Sample 1 maintains a higher $|Q_{R+}|$ than Sample 2 because the higher trapped charge density 1) increases the effective E-field across the FE layer by reducing the potential drop across the DE layer, and 2) screens the internal depolarization field more effectively, which stabilizes a higher $|Q_{R+}|$ for Sample 1. Because of the stronger E-field and screening effect, Sample 1 shows a larger Q change than Sample 2 as V_{SET} increases further into the high-V_{SET} region (V_{SET} = 7.1 V) [see Fig. 7(e)]. This divergence widens the Q_{R+} gap between the two samples, causing the final increase in $\sigma(Q_{R+})$ at the high-V_{SET}.

This "W"-shaped trend is most pronounced in scaled films (specifically, T_{FE} = 5 nm). As T_{FE} is reduced, $\sigma(Q_{R+})$ in the mid-V_{SET} region reduces, whereas that in the low- and high-V_{SET} regions remains approximately unchanged. Consequently, $\sigma(Q_{R+})$ in the mid-V_{SET} region becomes comparable in magnitude with that in the low- and high-V_{SET} regions as T_{FE} decreases, which makes the overall "W"-shaped $\sigma(Q_{R+})$-V_{SET} trend more pronounced.

D. Analysis of Factors Affecting Q_{R+} Variations Using 3-D Phase-Field Model

To gain further insights into the mechanisms governing the Q_{R+} variations, we utilize a calibrated 3-D phase-field model [34], [35] to simulate the MFIM structure. Our 3-D multigrain phase-field framework calculates the P profile in an MFIM stack by solving time-dependent Ginzburg–Landau (TDGL) and Poisson's equations. The model includes the polycrystalline nature of HZO by associating the 3-D grain-growth model with θ (details in [34] and [35]). It should be noted that the trap effect is not considered explicitly; instead, it is abstracted within calibrated parameters in the model. Thus, this model-based analysis sheds light only on the MD and polycrystallinity effects on the Q_{R+} variations. The black solid line in Fig. 8(a) represents the calibrated Q–V curve from the model for T_{FE} = 10 nm, which closely matches the average of measured Q–V curves over 50 MFIM capacitors

Authorized licensed use limited to: Purdue University. Downloaded on April 06,2026 at 18:00:14 UTC from IEEE Xplore. Restrictions apply.

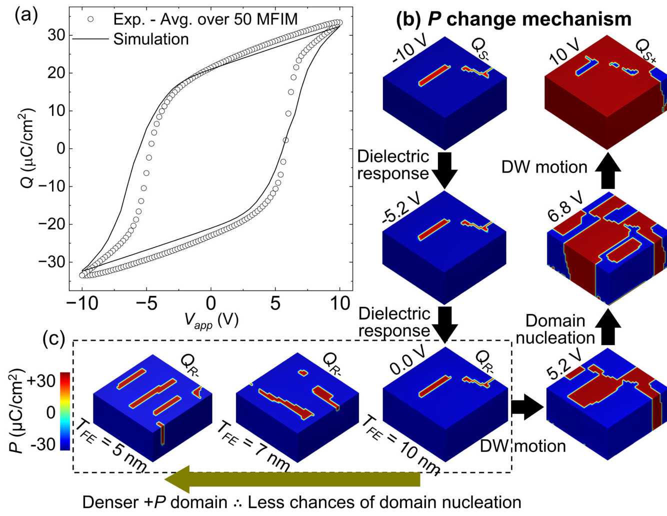

Fig. 8. (a) Simulated (line) and experimental (symbols) Q–V with T_{FE} = 10 nm. The experimental Q–V is averaged over 50 MFIM capacitors, (b) P maps from the phase-field simulation illustrating the P changing mechanism as V_{app} increases from −10 V (V_{RESET}) to 10 V (V_{SET}), and (c) simulated P maps of Q_{R-} for different (T_{FE} = 5, 7, and 10 nm).

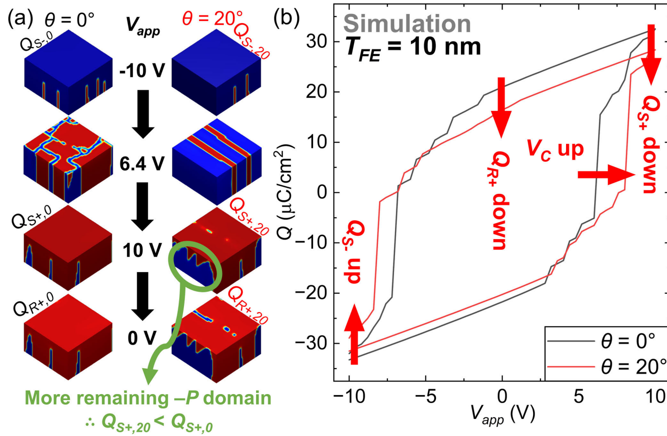

Fig. 9. (a) P maps during the V_{app} sweep (−10 V (V_{RESET}) → 10 V (V_{SET}) → 0 V) and (b) Q–V loops of HZO samples with θ = 0° and 20° from the phase-field simulations. $Q_{S-,\theta}$, $Q_{S+,\theta}$, and $Q_{R+,\theta}$ represent Q_{S-}, Q_{S+}, and Q_{R+} of the grain with grain orientation angle θ.

(black symbols). The P profiles from the phase-field simulation [see Fig. 8(b)] illustrate the voltage dependence of P switching mechanisms in the FE layer.

As expected, domain nucleation is observed at the V_{app} around the mid-V_{SET} range (5.2–6.8 V), which explains the significant variations observed in this region. The model also demonstrates a reduced chance of domain nucleation at smaller T_{FE} due to denser $+P$ domains at Q_{R-} [see Fig. 8(c)] [41]. These results are consistent with experimental data indicating the significant impact of domain nucleation on Q_{R+} variations in the mid-V_{SET} range and its dependence on T_{FE}. In low- and high-V_{SET} ranges, DE response and DW motion are prevalent mechanisms. As the randomness and magnitude in P switching reduce, the role of the MD effect in dictating Q_{R+} variations becomes marginal.

Our model suggests that grain angle variation due to polycrystallinity plays a key role in Q_{R+} variations in the low and high-V_{SET} regions (recall, traps are not included in our model). At V_{app} = 10 V, more $-P$ domains are observed in the grain with θ = 20° (compared to θ = 0°), leading to lower Q_{S+} [see Fig. 9(b)]. Since the DE response is prevalent during the backward V_{app} sweep from 10 to 0 V [see Fig. 9(a)], lower Q_{S+} directly leads to lower Q_{R+}. Likewise, in the low-V_{SET} range, polycrystallinity-induced Q_{S-} variations lead to Q_{R+} variations. Furthermore, our model predicts increased V_C in the grain with θ = 20° as discussed before. Therefore, our model corroborates the discussions in the previous sections that grains with larger θ exhibit smaller Q_{S+} and increased V_C.

Before concluding, we put the results into perspective for memory applications. The trends reported in this article have important implications for HZO-based memory read operation, especially for multilevel memories that program and sense intermediate P states. Even in a binary operation, the nonmonotonic dependence of $\sigma(Q_{R+})$ on V_{SET} is relevant for memory optimization because a practical write scheme may exploit intermediate states to reduce the required set voltage and switching energy. In this context, the broadened Q_{R+} distribution in the mid-V_{SET} range can degrade state distinguishability and thereby increase the error probability [50]. This variability is expected to be exacerbated in nanoscale devices, where statistical averaging over many grains is reduced, and the impact of structural nonuniformity becomes more pronounced [26]. Furthermore, the observed dependence of $\sigma(Q_{R+})$ on T_{FE}, specifically the suppression of variations in the mid-V_{SET} region with T_{FE} scaling, could have important implications for T_{FE} optimization. As discussed in [50], the reduction in $\sigma(Q_{R+})$ observed in thinner FE layers translates to lower error probability, which can outweigh the tradeoff of increased write-energy cost (due to an increase in capacitance with T_{FE} scaling). By experimentally confirming the dependence of $\sigma(Q_{R+})$ on T_{FE}, this work provides evidence that T_{FE} optimization is an effective knob for managing variations and enabling robust operation of HZO-based memories.

V. Conclusion

We experimentally investigated Q_R variations in HZO-based MFIM capacitors and their dependence on V_{SET} and T_{FE}. We established the experimental evidence of the previous simulation-based analysis showing the nonmonotonic behavior of $\sigma(Q_{R+})$ with V_{SET}. By analyzing the correlation between measured Q_R, V_C, and Q_S across different V_{SET} values, we identified the dominant factors governing Q_R variations. In the low- and high-V_{SET} regions, Q_{R+} variations are mainly driven by Q_{S+} variations. Our analysis suggests they originate from charge trapping at the FE–DE interface (as suggested by the positive correlation between measured values of dQ/dV_{app} and Q_{S+}) and polycrystalline effects due to grain angle variations (dominant at large T_{FE}) and *o*-/*t*-phase distribution (dominant at small T_{FE}). Conversely, near the mid-V_{SET} region, Q_{R+} variation is primarily dictated by V_C variation resulting from MD P switching combined with polycrystallinity. The random nature and sharp P switching associated with domain nucleation amplify the Q_{R+} variations, which lead to peaks in $\sigma(Q_{R+})$.

Authorized licensed use limited to: Purdue University. Downloaded on April 06,2026 at 18:00:14 UTC from IEEE Xplore. Restrictions apply.

This effect diminishes as T_{FE} decreases due to suppressed domain nucleation as well as reduced polycrystallinity. As a result, T_{FE} scaling reduces the peak variations in Q_{R+}.

References

[1] Y. Xu, *Ferroelectric Materials and Their Applications*. Amsterdam, The Netherlands: Elsevier, 2013.

[2] K. Uchino, *Ferroelectric Devices*. Boca Raton, FL, USA: CRC Press, Sep. 2018.

[3] N. Setter et al., "Ferroelectric thin films: Review of materials, properties, and applications," *J. Appl. Phys.*, vol. 100, no. 5, Sep. 2006, Art. no. 051606, doi: 10.1063/1.2336999.

[4] L. W. Martin and A. M. Rappe, "Thin-film ferroelectric materials and their applications," *Nature Rev. Mater.*, vol. 2, no. 2, pp. 1–14, Nov. 2016, doi: 10.1038/natrevmats.2016.87.

[5] T. S. Böscke, J. Müller, D. Bräuhaus, U. Schröder, and U. Böttger, "Ferroelectricity in hafnium oxide: CMOS compatible ferroelectric field effect transistors," in *IEDM Tech. Dig.*, Mar. 2011, pp. 24.5.1–24.5.4. [Online]. Available: https://ieeexplore.ieee.org/abstract/document/6131606

[6] S. Dünkel et al., "A FeFET based super-low-power ultra-fast embedded NVM technology for 22 nm FDSOI and beyond," in *IEDM Tech. Dig.*, Mar. 2017, pp. 19.7.1–19.7.4. [Online]. Available: https://ieeexplore.ieee.org/document/8268425/?arnumber=8268425

[7] T. Francois et al., "Demonstration of BEOL-compatible ferroelectric $Hf_{0.5}Zr_{0.5}O_2$ scaled FeRAM co-integrated with 130 nm CMOS for embedded NVM applications," in *IEDM Tech. Dig.*, Dec. 2019, pp. 15.7.1–15.7.4. [Online]. Available: https://ieeexplore.ieee.org/document/8993485/?arnumber=8993485

[8] J. Okuno et al., "SoC compatible 1T1C FeRAM memory array based on ferroelectric $Hf_{0.5}Zr_{0.5}O_2$," in *Proc. IEEE Symp. VLSI Technol.*, Jun. 2020, pp. 1–2. [Online]. Available: https://ieeexplore.ieee.org/document/9265063/?arnumber=9265063

[9] K. Ni et al., "Critical role of interlayer in $Hf_{0.5}Zr_{0.5}O_2$ ferroelectric FET nonvolatile memory performance," *IEEE Trans. Electron Devices*, vol. 65, no. 6, pp. 2461–2469, Jun. 2018. [Online]. Available: https://ieeexplore.ieee.org/document/8352114

[10] Y. Goh and S. Jeon, "The effect of the bottom electrode on ferroelectric tunnel junctions based on CMOS-compatible HfO_2," *Nanotechnology*, vol. 29, no. 33, Aug. 2018, Art. no. 335201. [Online]. Available: https://iopscience.iop.org/article/10.1088/1361-6528/aac6b3

[11] H. Ryu, H. Wu, F. Rao, and W. Zhu, "Ferroelectric tunneling junctions based on aluminum oxide/zirconium-doped hafnium oxide for neuromorphic computing," *Sci. Rep.*, vol. 9, no. 1, p. 20383, Dec. 2019. [Online]. Available: https://www.nature.com/articles/s41598-019-56816-x

[12] P. D. Lomenzo, Q. Takmeel, S. Moghaddam, and T. Nishida, "Annealing behavior of ferroelectric Si-doped HfO_2 thin films," *Thin Solid Films*, vol. 615, pp. 139–144, Sep. 2016. [Online]. Available: https://www.sciencedirect.com/science/article/pii/S0040609016303145

[13] B. Ku, Y. Ma, H. Han, W. Xuan, and C. Choi, "Effects of etching process and annealing temperature on the ferroelectric properties of atomic layer deposited al-doped HfO_2 thin film," *Nanotechnology*, vol. 33, no. 42, Oct. 2022, Art. no. 425205, doi: 10.1088/1361-6528/ac7cf7.

[14] J. Müller et al., "Ferroelectricity in yttrium-doped hafnium oxide," *J. Appl. Phys.*, vol. 110, no. 11, Dec. 2011, Art. no. 114113, doi: 10.1063/1.3667205.

[15] U. Schroeder et al., "Lanthanum-doped hafnium oxide: A robust ferroelectric material," *Inorganic Chem.*, vol. 57, no. 5, pp. 2752–2765, Mar. 2018, doi: 10.1021/acs.inorgchem.7b03149.

[16] R. Batra, T. D. Huan, G. A. Rossetti, and R. Ramprasad, "Dopants promoting ferroelectricity in hafnia: Insights from a comprehensive chemical space exploration," *Chem. Mater.*, vol. 29, no. 21, pp. 9102–9109, Nov. 2017, doi: 10.1021/acs.chemmater.7b02835.

[17] J. Müller et al., "Ferroelectricity in simple binary ZrO_2 and HfO_2," *Nano Lett.*, vol. 12, no. 8, pp. 4318–4323, Aug. 2012, doi: 10.1021/nl302049k.

[18] S. J. Kim et al., "Large ferroelectric polarization of TiN/$Hf_{0.5}Zr_{0.5}O_2$/TiN capacitors due to stress-induced crystallization at low thermal budget," *Appl. Phys. Lett.*, vol. 111, no. 24, Dec. 2017, Art. no. 242901, doi: 10.1063/1.4995619.

[19] N. Tasneem et al., "Trap capture and emission dynamics in ferroelectric field-effect transistors and their impact on device operation and reliability," in *IEDM Tech. Dig.*, Dec. 2021, pp. 6.1.1–6.1.4. [Online]. Available: https://ieeexplore.ieee.org/abstract/document/9720615

[20] Z. Wang et al., "Depolarization field induced instability of polarization states in HfO_2 based ferroelectric FET," in *IEDM Tech. Dig.*, Dec. 2020, pp. 4.5.1–4.5.4. [Online]. Available: https://ieeexplore.ieee.org/abstract/document/9372098

[21] P. Sharma et al., "Impact of total and partial dipole switching on the switching slope of gate-last negative capacitance FETs with ferroelectric hafnium zirconium oxide gate stack," in *Proc. Symp. VLSI Technol.*, 2017, pp. T154–T155. [Online]. Available: https://ieeexplore.ieee.org/abstract/document/7998160

[22] M. Pešić et al., "Variability sources and reliability of 3D-FeFETs," in *Proc. IEEE Int. Rel. Physics Symp. (IRPS)*, Mar. 2021, pp. 1–7. [Online]. Available: https://ieeexplore.ieee.org/abstract/document/9405118

[23] M. Pešić and B. Beltrando, "Embedding ferroelectric HfO_x in memory hierarchy: Material- defects–device entanglement," in *IEDM Tech. Dig.*, Dec. 2021, pp. 33.4.1–33.4.4. [Online]. Available: https://ieeexplore.ieee.org/abstract/document/9720623

[24] K. Chatterjee et al., "Challenges to partial switching of $Hf_{0.8}Zr_{0.2}O_2$ gated ferroelectric FET for multilevel/analog or low-voltage memory operation," *IEEE Electron Device Letters*, vol. 40, no. 9, pp. 1423–1426, Sep. 2019. [Online]. Available: https://ieeexplore.ieee.org/document/8777131/?arnumber=8777131

[25] T. Ali et al., "A multilevel FeFET memory device based on laminated HSO and HZO ferroelectric layers for high-density storage," in *IEDM Tech. Dig.*, Dec. 2019, pp. 28.7.1–28.7.4. [Online]. Available: https://ieeexplore.ieee.org/document/8993642/?arnumber=8993642

[26] K. Ni, W. Chakraborty, J. A. Smith, B. Grisafe, and S. Datta, "Fundamental understanding and control of device-to-device variation in deeply scaled ferroelectric FETs," in *Proc. Symp. VLSI Technol.*, Jun. 2019, pp. T40–T41. [Online]. Available: https://ieeexplore.ieee.org/document/8776497

[27] M. Jerry et al., "Ferroelectric FET analog synapse for acceleration of deep neural network training," in *IEDM Tech. Dig.*, 2017, pp. 6.2.1–6.2.4. [Online]. Available: https://ieeexplore.ieee.org/abstract/document/8268338

[28] M. Jerry et al., "A ferroelectric field effect transistor based synaptic weight cell," *J. Phys. D, Appl. Phys.*, vol. 51, no. 43, Oct. 2018, Art. no. 434001, doi: 10.1088/1361-6463/aad6f8.

[29] S. Dutta et al., "Biologically plausible ferroelectric quasi-leaky integrate and fire neuron," in *Proc. Symp. VLSI Technol.*, 2019, pp. T140–T141. [Online]. Available: https://ieeexplore.ieee.org/document/8776487/?arnumber=8776487

[30] M. H. Park et al., "Surface and grain boundary energy as the key enabler of ferroelectricity in nanoscale hafnia-zirconia: A comparison of model and experiment," *Nanoscale*, vol. 9, no. 28, pp. 9973–9986, 2017. [Online]. Available: https://pubs.rsc.org/en/content/articlelanding/2017/nr/c7nr02121f

[31] S. D. Hyun et al., "Dispersion in ferroelectric switching performance of polycrystalline $Hf_{0.5}Zr_{0.5}O_2$ thin films," *ACS Appl. Mater. Interface*, vol. 10, no. 41, pp. 35374–35384, Oct. 2018, doi: 10.1021/acsami.8b13173.

[32] C. Garg et al., "Impact of random spatial fluctuation in non-uniform crystalline phases on the device variation of ferroelectric FET," *IEEE Electron Device Letters*, vol. 42, no. 8, pp. 1160–1163, Aug. 2021. [Online]. Available: https://ieeexplore.ieee.org/abstract/document/9448048

[33] T. K. Paul, A. K. Saha, and S. K. Gupta, "Direction-dependent lateral domain walls in ferroelectric hafnium zirconium oxide and their gradient energy coefficients: A first-principles study," *Adv. Electron. Mater.*, vol. 10, no. 1, Jan. 2024, Art. no. 2300400. [Online]. Available: https://onlinelibrary.wiley.com/doi/pdf/10.1002/aelm.202300400

[34] R. Koduru, A. K. Saha, M. Si, X. Lyu, P. D. Ye, and S. K. Gupta, "Variation and stochasticity in polycrystalline HZO based MFIM: Grain-growth coupled 3D phase field model based analysis," in *IEDM Tech. Dig.*, Dec. 2021, pp. 15.2.1–15.2.4. [Online]. Available: https://ieeexplore.ieee.org/abstract/document/9720564

[35] R. Koduru, I. Ahmed, A. K. Saha, X. Lyu, P. Ye, and S. K. Gupta, "Phase-field simulations of polarization variations in polycrystalline $Hf_{0.5}Zr_{0.5}O_2$ based MFIM: Voltage dependence and dynamics," *J. Appl. Phys.*, vol. 134, no. 8, Aug. 2023, Art. no. 084104, doi: 10.1063/5.0158997.

[36] M. Si, X. Lyu, and P. D. Ye, "Ferroelectric polarization switching of hafnium zirconium oxide in a ferroelectric/dielectric stack," *ACS Appl. Electron. Mater.*, vol. 1, no. 5, pp. 745–751, May 2019, doi: 10.1021/acsaelm.9b00092.

Authorized licensed use limited to: Purdue University. Downloaded on April 06,2026 at 18:00:14 UTC from IEEE Xplore. Restrictions apply.

[37] Y. Qu, J. Li, M. Si, X. Lyu, and P. D. Ye, "Quantitative characterization of interface traps in ferroelectric/dielectric stack using conductance method," *IEEE Trans. Electron Devices*, vol. 67, no. 12, pp. 5315–5321, Dec. 2020. [Online]. Available: https://ieeexplore.ieee.org/abstract/document/9257406

[38] J. Li, M. Si, Y. Qu, X. Lyu, and P. D. Ye, "Quantitative characterization of ferroelectric/dielectric interface traps by pulse measurements," *IEEE Trans. Electron Devices*, vol. 68, no. 3, pp. 1214–1220, Mar. 2021. [Online]. Available: https://ieeexplore.ieee.org/document/9344681

[39] R. Materlik, C. Künneth, and A. Kersch, "The origin of ferroelectricity in $Hf_{1-x}Zr_xO_2$: A computational investigation and a surface energy model," *J. Appl. Phys.*, vol. 117, no. 13, Apr. 2015, Art. no. 134109, doi: 10.1063/1.4916707.

[40] C. Künneth, R. Materlik, and A. Kersch, "Modeling ferroelectric film properties and size effects from tetragonal interlayer in $Hf_{1-x}Zr_xO_2$ grains," *J. Appl. Phys.*, vol. 121, no. 20, May 2017, Art. no. 205304, doi: 10.1063/1.4983811.

[41] A. Saha, M. Si, K. Ni, S. Datta, P. D. Ye, and S. K. Gupta, "Ferroelectric thickness dependent domain interactions in FEFETs for memory and logic: A phase-field model based analysis," in *IEDM Tech. Dig.*, Dec. 2020, pp. 4.3.1–4.3.4.

[42] Y. Park, W. Park, and S. Kim, "Enhancing ferroelectricity in $HfAlO_x$-based ferroelectric tunnel junctions: A comparative study of MFS and MFIS structures with ultrathin interfacial layers," *Ceram. Int.*, vol. 50, no. 15, pp. 26849–26857, Aug. 2024. [Online]. Available: https://www.sciencedirect.com/science/article/pii/S0272884224018376

[43] H. Chen et al., "Significant improvement of ferroelectricity and reliability in $Hf_{0.5}Zr_{0.5}O_2$ films by inserting an ultrathin Al_2O_3 buffer layer," *Appl. Surf. Sci.*, vol. 542, Mar. 2021, Art. no. 148737. [Online]. Available: https://www.sciencedirect.com/science/article/pii/S0169433220334966

[44] N. Siannas et al., "Metastable ferroelectricity driven by depolarization fields in ultrathin $Hf_{0.5}Zr_{0.5}O_2$," *Commun. Phys.*, vol. 5, no. 1, p. 178, Jul. 2022.

[45] A. K. Saha, M. Si, P. D. Ye, and S. K. Gupta, "Polarization switching in $Hf_{0.5}Zr_{0.5}O_2$-dielectric stack: The role of dielectric layer thickness," *Appl. Phys. Lett.*, vol. 119, no. 12, Sep. 2021, Art. no. 122903.

[46] J. G. Simmons, "Generalized formula for the electric tunnel effect between similar electrodes separated by a thin insulating film," *J. Appl. Phys.*, vol. 34, no. 6, pp. 1793–1803, 1963.

[47] G. A. M. Hurkx, D. B. M. Klaassen, and M. P. G. Knuvers, "A new recombination model for device simulation including tunneling," *IEEE Trans. Electron Devices*, vol. 39, no. 2, pp. 331–338, Feb. 1992.

[48] J. Barbot et al., "Interplay between charge trapping and polarization switching in MFDM stacks evidenced by frequency-dependent measurements," in *Proc. ESSCIRC*, 2022, pp. 125–128. [Online]. Available: https://ieeexplore.ieee.org/document/9911485/?arnumber=9911485

[49] M. Hoffmann et al., "Stabilizing the ferroelectric phase in doped hafnium oxide," *J. Appl. Phys.*, vol. 118, no. 7, Aug. 2015, Art. no. 072006, doi: 10.1063/1.4927805.

[50] R. Koduru, T. K. Paul, and S. K. Gupta, "Variability in ferroelectric $Hf_{0.5}Zr_{0.5}O_2$: Physical insights and implications for memory applications," in *Proc. Device Res. Conf. (DRC)*, Jun. 2025, pp. 1–2.

Authorized licensed use limited to: Purdue University. Downloaded on April 06,2026 at 18:00:14 UTC from IEEE Xplore. Restrictions apply.